JOURNAL OF GEOPHYSICAL RESEARCH: OCEANS, VOL. 119, 359–376, doi:10.1002/2013JC009246, 2014

On the spatial and temporal distribution of near-inertial energy in the Southern Ocean

Willi Rath,[1] Richard J. Greatbatch,[1] and Xiaoming Zhai[2]

Received 1 July 2013; revised 11 November 2013; accepted 23 December 2013; published 16 January 2014.

[1] We use an eddying realistic primitive-equation model of the Southern Ocean to examine the spatial and temporal distribution of near-inertial wind-power input (WPI) and near-inertial energy (NIE) in the Southern Ocean. We find that the modeled near-inertial WPI is almost proportional to inertial wind-stress variance (IWSV), while the modeled NIE is modulated by the inverse of the mixed-layer depth. We go on to assess recent decadal trends of near-inertial WPI from trends of IWSV based on reanalysis wind stress. Averaged over the Southern Ocean, annual-mean IWSV is found to have increased by 16% over the years 1979–2011. Part of the increase of IWSV is found to be related to the positive trend of the Southern-Annular Mode over the same period. Finally, we show that there are horizontal local maxima of NIE at depth that are almost exclusively associated with anticyclonic eddies.

Citation: Rath, W., R. J. Greatbatch, and X. Zhai (2014), On the spatial and temporal distribution of near-inertial energy in the Southern Ocean, *J. Geophys. Res. Oceans*, *119*, 359–376, doi:10.1002/2013JC009246.

1. Introduction

[2] Near-inertial waves (NIWs) play a key role in the global climate system. By deepening the oceanic mixed layer [*Pollard et al*., 1972], they influence the global sea-surface temperature and especially in the tropics, by teleconnections, potentially have a global impact on the atmospheric circulation [*Jochum et al*., 2013]. The contribution of wind-generated NIWs to the energy available for mixing at depth, which is thought to drive the global overturning circulation [*Munk and Wunsch*, 1998], is a matter of debate. Model-based estimates of global near-inertial wind-power input (WPI) are of the order of 0.5 TW [*Watanabe and Hibiya*, 2002; *Alford*, 2003; *Furuichi et al*., 2008] with large uncertainties stemming from a high sensitivity to the spatial and temporal resolution of the wind stress used to force the model [*Jiang et al*., 2005], from missing physics in the simple models [*Plueddemann and Farrar*, 2006] and from the wind-stress parameterization [*Rath et al*., 2013]. Direct global observational estimates of NIWs are restricted to the ocean surface [*Chaigneau et al*., 2008; *Elipot and Lumpkin*, 2008], and observations of NIWs at depth are only available at a limited number of locations [*Pollard and Millard*, 1970; *D'Asaro*, 1985; *Alford*, 2003; *Plueddemann and Farrar*, 2006].

[3] Recent modeling studies show that the majority of the wind-induced near-inertial energy (NIE) is dissipated within the surface-mixed layer and estimate that only approximately 20% of the NIE injected at the surface is able to escape the mixed layer and contribute to mixing in the ocean interior [*Furuichi et al*., 2008; *Zhai et al*., 2009]. Anticyclonic eddies are known to trap NIWs [*Kunze*, 1985; *Zhai et al*., 2005] and provide a possible pathway to the interior ocean [*Zhai et al*., 2007; *Jing et al*., 2011]. However, the relevance of anticyclonic eddies for determining the fraction of NIE available for mixing at depth has yet to be quantified.

[4] In this study, we use a realistic primitive-equation model at eddying spatial resolution to examine the spatial and temporal distribution of near-inertial WPI and NIE in the Southern Ocean. After describing details on the model and the data in section 2, we present our results for the large-scale spatial distribution of near-inertial WPI and NIE and assess the relevance of enhanced NIE in anticyclonic eddies in section 3. We proceed to the annual cycle in section 4. Section 5 highlights the relation of inertial wind-stress variance (IWSV) to near-inertial WPI and NIE in the mixed layer. In section 6, we assess recent decadal trends of IWSV and use the relationship to modeled near-inertial WPI to assess the implications for NIWs in the ocean. We close with a summary in section 7.

2. Methods, Models, and Data

2.1. Primitive-Equation Model

[5] We use an eddying $(1/10)^\circ$ regional setup of SPFLAME [*Eden*, 2006], a primitive-equation ocean model which goes back to Modular Ocean Model 2 (MOM2) [*Pacanowski*, 1996]. The configuration is identical to the one described by *Rath et al*. [2013]. It covers all the

[1]GEOMAR Helmholtz Centre for Ocean Research Kiel, Kiel, Germany.
[2]Centre for Ocean and Atmospheric Sciences, School of Environmental Sciences, University of East Anglia, Norwich, UK.

Corresponding author: W. Rath, GEOMAR Helmholtz Centre for Ocean Research Kiel, Duesternbrooker Weg 20, DE-24105 Kiel, Germany. (wrath@geomar.de)

2169-9275/14/10.1002/2013JC009246

Southern Ocean south of 30°S and has a realistic topography. The model is driven by realistic wind stress derived from six-hourly wind fields using the surface-velocity-dependent parameterization described by *Duhaut and Straub* [2006] and *Rath et al*. [2013]

$$\boldsymbol{\tau}_{SVD} \equiv \rho_a c_d(|\boldsymbol{U}_{10} - \boldsymbol{u}_o|)|\boldsymbol{U}_{10} - \boldsymbol{u}_o|(\boldsymbol{U}_{10} - \boldsymbol{u}_o), \tag{1}$$

where $\boldsymbol{u}_o$ is the surface velocity, $\boldsymbol{U}_{10}$ is 10 m wind from the ERA-40 reanalysis [*Uppala et al*., 2005], ρ_a is the density of air close to the sea surface, and $c_d(U)$ is the drag coefficient given by the formula of *Large and Pond* [1981] modified at large values of U according to *Donelan et al*. [2004]. Surface-heat flux is prescribed using a climatology [*Barnier et al*., 1995]. Surface salinity is restored to climatological values with a time scale of 15 days for the upper level of thickness 10 m. Horizontal mixing is parameterized in both the momentum and tracer equation using a biharmonic diffusivity.

[6] Vertical mixing is parameterized using the turbulent-kinetic-energy (TKE) mixing scheme described by *Gaspar et al*. [1990] and *Blanke and Delecluse* [1993]. The scheme parameterizes the vertical fluxes as eddy diffusivities that depend on the TKE. TKE, in turn, is calculated from a prognostic equation where vertical shear of horizontal velocity acts to increase, and strong stratification acts to reduce TKE [*Gaspar et al*., 1990]. The TKE scheme has been shown to reproduce the seasonality of the near-surface temperature at station Papa in the Gulf of Alaska and to reproduce the evolution of near-inertial energy at the Long-Term Upper Ocean Study site in the Sargasso Sea by *Gaspar et al*. [1990].

[7] The model is spun up for 31 years from a state of rest and hydrography specified from climatology. The first 10 years of the spin-up are driven by climatological wind stress that neglects the ocean-surface velocity, and the following 21 years of the spin-up are driven by six-hourly ERA-40-based wind stress parameterized according to

$$\boldsymbol{\tau}_{CTL} \equiv \rho_a c_d(|\boldsymbol{U}_{10}|)|\boldsymbol{U}_{10}|\boldsymbol{U}_{10}. \tag{2}$$

[8] The model shows a realistic Antarctic Circumpolar Current (ACC), and a realistic mesoscale eddy field [*Eden*, 2006; *Rath et al*., 2013].

[9] After the spin-up, and starting on 1 January 2001, the wind-stress parameterization is changed to include the ocean-surface velocity according to (1). Note that we start the analysis of the model output immediately after changing the wind-stress parameterization to surface-velocity-dependent and that, consequently, the adjustment of the model to the new wind-stress parameterization is contained in the data we present here. *Rath et al*. [2013] showed that surface-velocity-dependent wind stress acts to significantly reduce NIE in the mixed layer as well as at depth and that this reduction spreads from the surface to depth within approximately a month. Hence, we expect that during the first month of the model output presented here, NIE especially at depth is overestimated. The focus of this study, however, is on near-inertial WPI and on mixed-layer NIE, which adjust to surface-velocity-dependent wind stress on time scales much shorter than a month.

[10] The first 36.5 days of the model output for the year 2001 are available at the full spatial resolution of the model ($1/10° \times 1/10°$) and at a temporal resolution of 3 h. For the rest of the year 2001, the spatial resolution of the model output was reduced to $1° \times 1°$ without changing the temporal resolution. By comparing the full-resolution output for the first 36.5 days to the reduced-resolution output over the same period, it was confirmed that near-inertial WPI and NIE at the reduced spatial resolution contain all the information that is relevant for this study. Apart from the discussion of the effect of anticyclonic eddies in section 3.1, all the analysis presented here is based on the reduced-resolution output.

2.2. Near-Inertial Quantities

[11] We separate the velocity field into the subinertial, the near-inertial, and the superinertial frequency band. The subscript I indicates near-inertial quantities, and the subscripts S and T indicate subinertial and superinertial quantities, respectively. In the actual calculations, the separation into the three frequency bands was realized using a fifth-order Butterworth filter as described in *Rath et al*. [2013].

[12] We define NIE as

$$E_I \equiv \rho_0 \frac{\boldsymbol{u}_I \cdot \boldsymbol{u}_I}{2}, \tag{3}$$

the mixed-layer NIE as the integral

$$E_{I,ML} \equiv \int_{-H}^{0} E_I(z)\mathrm{d}z, \tag{4}$$

where $\boldsymbol{u}_I$ is the near-inertially filtered velocity and H is the mixed-layer depth (see section 2.5). Finally, we define near-inertial WPI as

$$WPI_I \equiv \boldsymbol{\tau} \cdot \boldsymbol{u}_I(z = 0). \tag{5}$$

2.3. Simplified Models for Near-Inertial Wind-Power Input and Near-Inertial Energy

[13] *Pollard and Millard* [1970] proposed a local linear slab-ocean model for near-inertial oscillations (PM70) which has since been widely used to assess the input of near-inertial energy into the surface-mixed layer of the ocean [see, e.g., *Alford*, 2003]. PM70 is a local model for the near-inertial velocity in the mixed layer (u, v), which is assumed to be vertically uniform. It features the Coriolis force $f(-v, u)$, the wind stress $\boldsymbol{\tau} = (\tau^x, \tau^y)$, a linear damping term with the coefficient ε, the mixed-layer depth H (assumed to be time-independent), and the reference density ρ_0:

$$u_t - fv = \frac{\tau^x}{\rho_0 H} - \varepsilon u, \tag{6}$$

$$v_t + fu = \frac{\tau^y}{\rho_0 H} - \varepsilon v. \tag{7}$$

[14] The time evolution of kinetic energy, $E = \rho_0 \boldsymbol{u} \cdot \boldsymbol{u}/2$, in PM70 is governed by

$$\frac{E_t}{\rho_0} = uu_t + vv_t = \frac{1}{\rho_0 H}(\tau^x u + \tau^y v) - \varepsilon(u^2 + v^2). \tag{8}$$

[15] With given mixed-layer depth H, ε is the only free parameter of the model. It is usually tuned to minimize the

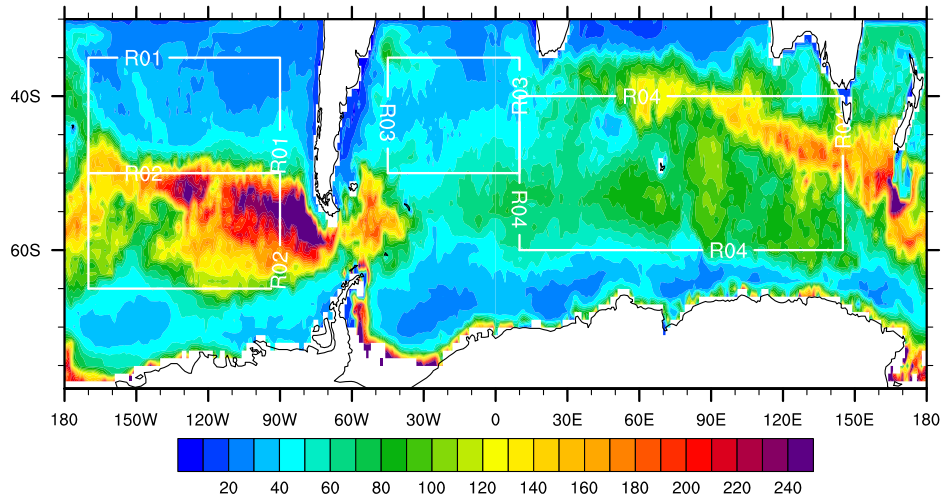

Figure 1. Year 2001 time-averaged mixed-layer depth H (m) diagnosed from the primitive-equation-model potential density σ_0 as discussed in the text. Also shown are the regions R01–R04 referred to in the text.

difference between modeled currents, the modeled near-inertial WPI or the modeled NIE, and observations. Typically, tuned $1/\varepsilon$ is found to be in the range of 2–10 days [see, e.g., *Pollard and Millard*, 1970; *D'Asaro*, 1985].

[16] In this study, we do not use PM70 to directly assess the oceanic response to high-frequency wind forcing, and in fact, it has been shown that PM70 has its shortcomings (see the next paragraph). However, in section 5.1, the ratio of time-averaged NIE and near-inertial WPI will be examined, and the scaling of this ratio in PM70 is a useful reference point. Setting E_t to zero in (8) and using (3) and (5) leads to

$$\frac{\overline{E_I}}{\overline{WPI_I}} = \frac{1}{2\varepsilon H} \propto \frac{1}{H}, \tag{9}$$

and to

$$\frac{\overline{E_I} \cdot H}{\overline{WPI_I}} = \frac{1}{2\varepsilon}, \tag{10}$$

where $\overline{(\ldots)}$ denotes temporal averaging. We shall return to the relationships given by (9) and (10) in section 5.1.

[17] *Plueddemann and Farrar* [2006] examine the performance of PM70 and of a mixed-layer model (PWP) similar to the one described by *Price et al*. [1986] that features a vertically uniform slab on top of a transition zone where free convective mixing, mixed-layer entrainment, and shear instability can alter the mixed-layer depth. *Plueddemann and Farrar* [2006] added a linear damping term mimicking the radiation of NIWs away from the mixed layer and acting on similar time scales as the linear damping term of PM70. In PWP, mixed-layer entrainment and mixing driven by shear instability are parameterized using two different Richardson number criteria, both relating stratification to velocity shear at the base of the mixed layer. Comparing PM70 and PWP model results to observed near-inertial currents from mooring sites, *Plueddemann and Farrar* [2006] found PM70 to be unable to reproduce the observed near-inertial WPI and NIE at the same time because it lacked an energy sink acting on time scales shorter than those associated with ε. PWP, on the other hand, correctly captured the observed energy balance on all time scales.

2.4. Regions and Seasons

[18] We separate the model domain into four regions shown as white boxes in Figure 1.

R01: $x \in (190°\text{E}, 270°\text{E})$ and $y \in (50°\text{S}, 35°\text{S})$
R02: $x \in (190°\text{E}, 270°\text{E})$ and $y \in (65°\text{S}, 50°\text{S})$
R03: $x \in (315°\text{E}, 10°\text{E})$ and $y \in (50°\text{S}, 35°\text{S})$
R04: $x \in (10°\text{E}, 145°\text{E})$ and $y \in (60°\text{S}, 40°\text{S})$

[19] The regions were chosen to take account of the large spatial differences of the mixed-layer depth (see Figures 6 and 8d).

[20] For the seasons, we use the oceanographic convention with boreal winter/austral summer comprising the months January–March (JFM), boreal spring/austral fall comprising April–June (AMJ), boreal summer/austral winter comprising the months July–September (JAS), and boreal fall/austral spring comprising the months October–December (OND).

2.5. Mixed-Layer Depth

[21] The vertical distribution of NIE is separated into high levels of NIE that are confined to a surface layer and into lower levels of NIE below. The depth of this surface layer is often approximated by the mixed-layer depth derived from hydrographic criteria (*de Boyer Montegut et al*. [2004] list various criteria used in the literature). If not stated otherwise, we will use the depth H at which the monthly-mean potential density σ_0 first exceeds the value at the surface by 0.03 kg/m^3. Note that in this study, we diagnose mixed-layer NIE, defined in (4), using this monthly-mean definition of the mixed-layer depth. We did test different definitions of the mixed-layer depth (different temporal resolutions and different density and temperature difference criteria) and found the vertical integral of NIE in the surface-mixed layer to be relatively insensitive to the

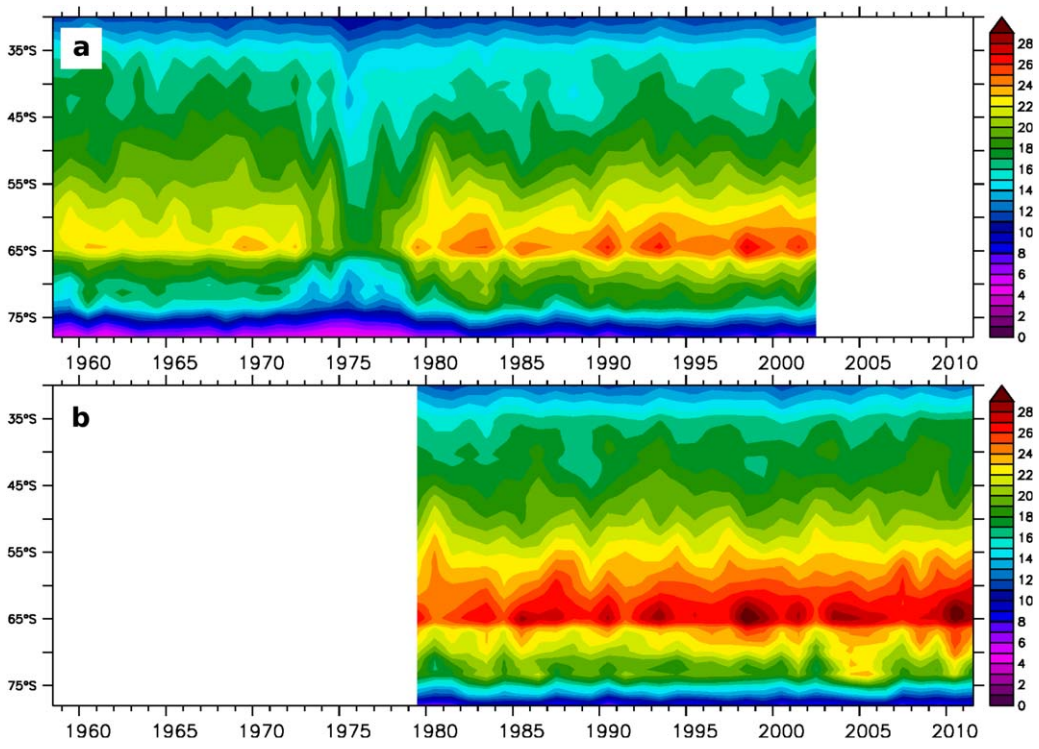

Figure 2. Annual and zonal averages of UVAR5 in m^2/s^2 (see text) for (a) ERA-40 and (b) ERA-Interim.

exact definition of H even on time scales of days (see section 5.1).

[22] In the Southern Ocean, a deep mixed layer along the path of the Antarctic Circumpolar Current (reaching more than 300 m in the annual average) is flanked by a shallower mixed layer (up to 50 m in the north and up to 100 m in the south). The modeled annual-mean mixed-layer depth shown in Figure 1 broadly agrees with the climatological estimate provided by *de Boyer Montegut et al*. [2004] (not shown). Depending on the region, the austral-winter mixed-layer depth can be more than ten times deeper than the austral-summer mixed-layer depth (see Figure 8d which is discussed later).

2.6. Inertial Wind-Stress Variance

[23] We define the inertial wind-stress variance

$$\mathrm{IWSV} \equiv |\tilde{\tau}_I^x|^2 + |\tilde{\tau}_I^y|^2, \tag{11}$$

where $\tilde{\tau}_I^x$ and $\tilde{\tau}_I^y$ are the Fourier transforms of the wind-stress components τ^x and τ^y at the (latitude-dependent) inertial frequency, respectively. We calculate monthly values for IWSV by calculating the Fourier transforms $\tilde{\tau}_I^x$ and $\tilde{\tau}_I^y$ based on six-hourly wind stress separately for each month. We tried different proxies for the wind-stress variability on inertial time scales and found the results of this study to be hardly affected. We will give IWSV in arbitrary units that are, however, consistent throughout this study.

2.7. Choosing the Wind Product

[24] Figure 2 compares the annually and zonally averaged variances of zonal 10 m wind on time scales shorter than 5 days (UVAR5) for ERA-40 and for ERA-Interim. For ERA-40, UVAR5 for the presatellite era (before 1979) is significantly lower than UVAR5 later on. There is a notable decrease of UVAR5 for the years 1973–1978 of ERA-40. UVAR5 from ERA-Interim is higher than UVAR5 from ERA-40 in the years present in both products. The spatial and temporal variability of UVAR5 in ERA-Interim and ERA-40, however, broadly agrees. The spatial resolution of the ERA-Interim fields is approximately $0.7°\times0.7°$, and the spatial resolution of the ERA-40 fields is approximately $1.125°\times1.125°$. We attribute the higher UVAR5 of ERA-Interim to the higher spatial resolution of the ERA-Interim wind fields [see also *Jiang et al*., 2005]. In this study, we only use post-1979 reanalysis winds.

2.8. Southern-Annular Mode

[25] We calculate the Southern-Annular-Mode (SAM) index using an ad hoc definition [*Gong and Wang*, 1999] based on the difference of monthly-mean zonally averaged sea-level pressure at 65°S and at 40°S. The annual-mean SAM index is obtained by annually averaging the monthly SAM index. There is broad agreement with the station-based SAM index presented by *Visbeck* [2009] (Figure 3a). The regression of the annual-mean zonal 10 m wind anomalies onto the annual-mean SAM index (Figure 3b) is dominated by a largely zonal pattern of positive wind anomalies between 65°S and 45°S.

3. Spatial Distribution of Near-Inertial Wind-Power Input and Near-Inertial Energy

3.1. Horizontal Distribution

[26] The large-scale spatial patterns of time-averaged near-inertial WPI and mixed-layer NIE for the whole year

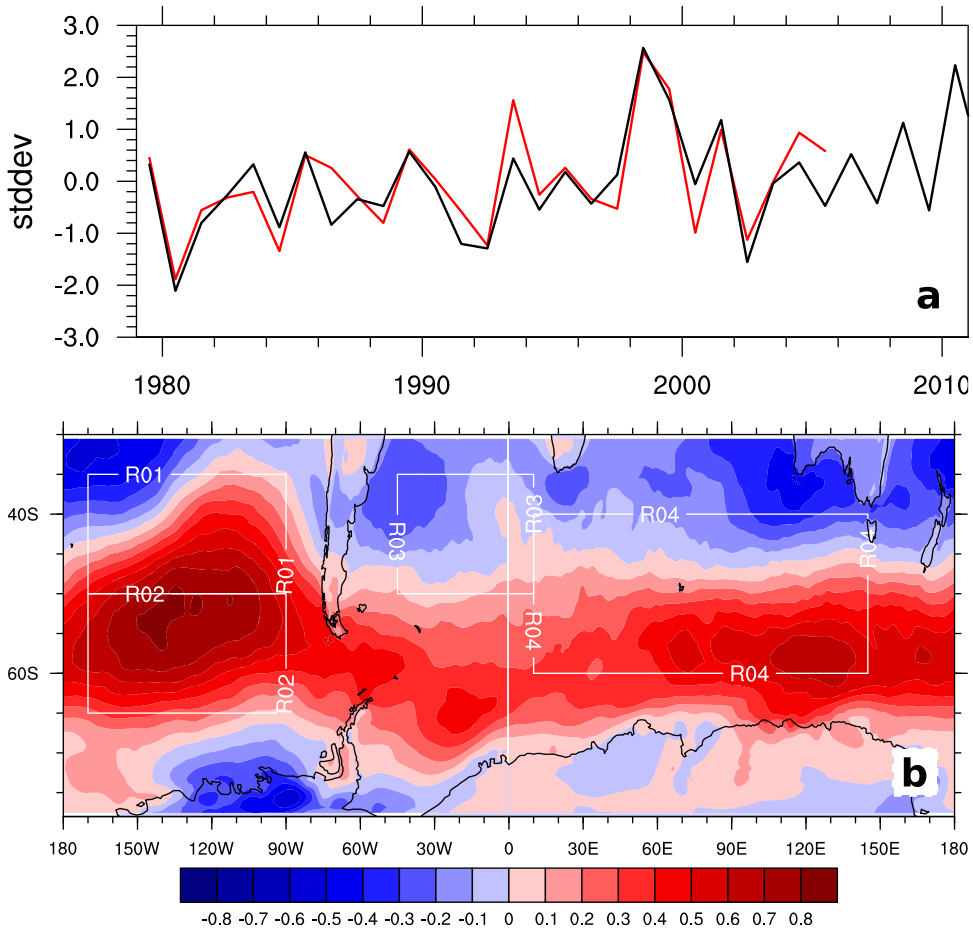

Figure 3. (a) Annual-mean SAM index calculated from ERA-Interim (black line) and from *Visbeck* [2009] (red line). (b) SAM-related annual-mean zonal wind pattern (m/s).

2001 are generally different (Figure 4). While near-inertial WPI is dominated by a largely zonal structure with meridional maxima between 65°S and 40°S, high levels of mixed-layer NIE are mainly found north of 55°S. Figure 5 shows the 2001 seasonal averages (JFM, etc.) of near-inertial WPI and mixed-layer NIE. As for the whole-year average, seasonally averaged near-inertial WPI shows a banded structure following the southern-hemisphere storm track with superimposed smaller local maxima that are often less than 5° in diameter (see, e.g., region R01 in JAS). The spatial distribution of seasonally averaged mixed-layer NIE, on the other hand, is more obviously characterized by structures less than 5° in diameter. Again, the zonal structure of near-inertial WPI is not reflected by the mixed-layer NIE, but on spatial scales of a few degrees, local maxima of mixed-layer NIE often agree with local maxima of near-inertial WPI. However, there are strong maxima in near-inertial WPI that are not associated with high mixed-layer NIE.

[27] While in regions R01, R03, and R04 (see section 2.4 and Figure 1) high near-inertial WPI leads to high levels of mixed-layer NIE, there is a discrepancy between near-inertial WPI and mixed-layer NIE in R02 which covers the Pacific sector of the ACC. In R02, even when near-inertial WPI is large compared to the spatial average over the whole model domain, mixed-layer NIE levels remain low. This difference is most pronounced in austral winter (JAS), when the high near-inertial WPI in the Pacific sector of the ACC (R02) is not reflected by the mixed-layer NIE. The difference of the horizontal distribution of the time averages of the modeled NIE and near-inertial WPI will be related to the different time scales governing the temporal evolution of near-inertial WPI and NIE in section 5.

3.2. Strength of the Modeled NIWs Compared to Observations

[28] It is known that forcing an ocean model with a wind stress that is sampled at a finite frequency leads to an underestimation of the near-inertial current amplitudes [*Niwa and Hibiya*, 1999; *Watanabe and Hibiya*, 2002; *Alford*, 2003]. *Niwa and Hibiya* [1999] showed using an analytic approach that in the linear slab-ocean model of *Pollard and Millard* [1970], a six-hourly wind-stress forcing leads to an underestimation of the resulting near-inertial amplitudes by a factor of approximately 1/1.4 at 40°S and 1/2.2 at 70°S. Consequently, NIE in the linear slab-ocean model is expected to be underestimated by 50% at 40°S and by even more south of that.

[29] As was stated in section 1, there are few observational estimates of NIE at a global scale. *Elipot and Lumpkin* [2008] present an estimate of the zonally averaged velocity variance in the near-inertial frequency band that is based

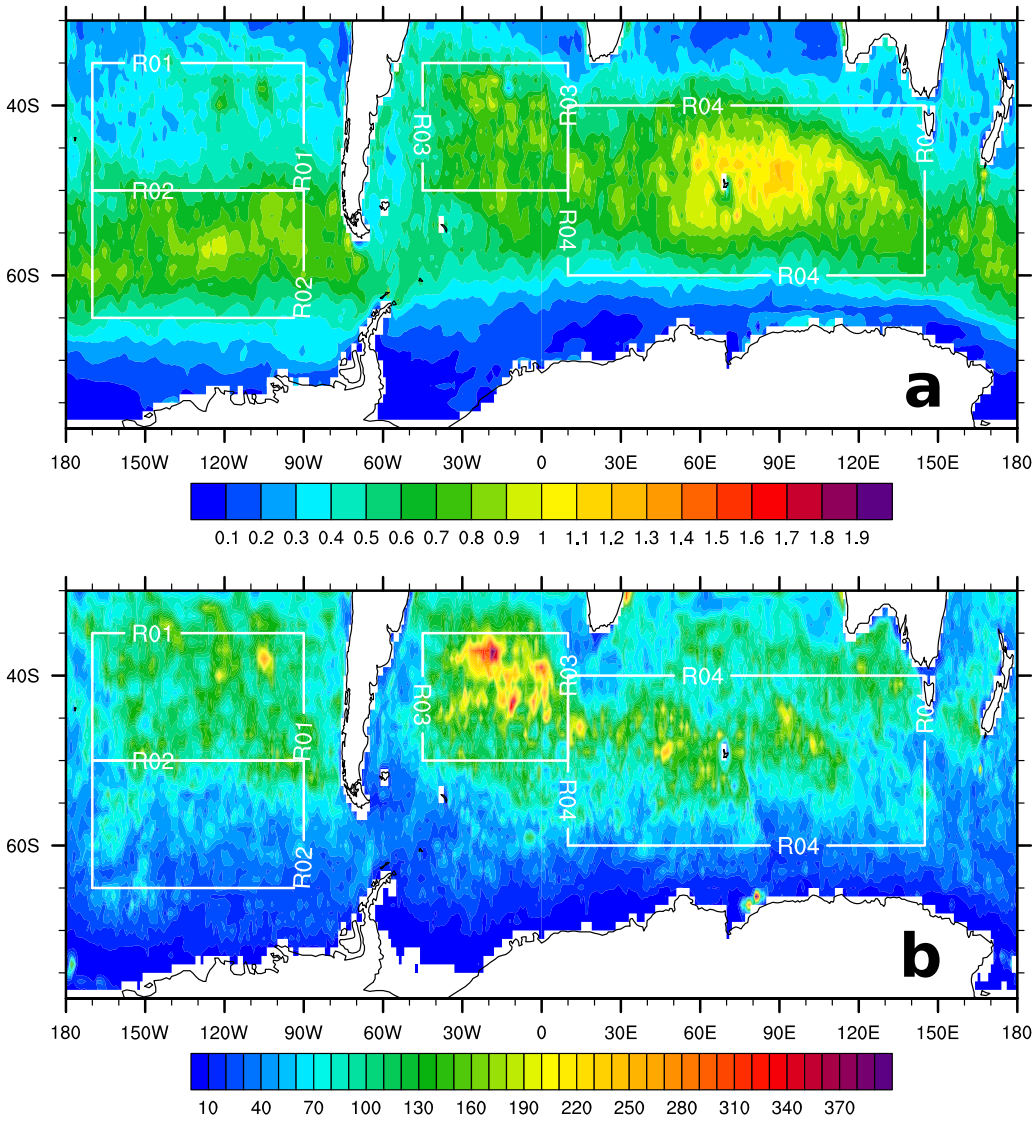

Figure 4. Year 2001 time averages of (a) near-inertial WPI (mW/m^2) and (b) mixed-layer NIE (J/m^2).

on drifter data. At approximately 40°S, they find the near-inertial velocity variance to be approximately 0.02 m^2/s^2. Multiplied by ρ_0 and divided by two, this translates to a near-surface NIE density of approximately 10 J/m^3. In our model, the temporally and zonally averaged NIE density at the surface ranges from below 1 J/m^3 south of approximately 55°S to 4.5 J/m^3 around 40°S. We conclude that in accord with the estimates of *Niwa and Hibiya* [1999], our model is likely to underestimate NIE at 40°S by approximately 50%.

3.3. Vertical Distribution

[30] Figure 6 shows the primitive-equation-model horizontal and seasonal averages of NIE, of potential density referenced to the surface (σ_0), of the mixed-layer depth defined as in section 2.5, and of the penetration depth of NIE, defined as the depth at which NIE has decayed to 50% of its value at the surface, for each of the four regions. The assumption of PM70, that NIE is concentrated in a layer close to the surface, generally holds, and in fact, the values of NIE in the mixed layer are often higher than the values of NIE below by several orders of magnitude. Furthermore, we note that the seasonally and horizontally averaged mixed-layer depth often is a good approximation for the penetration depth of seasonally and horizontally averaged wind-induced NIE.

[31] Horizontally and temporally averaged NIE within the mixed layer is not vertically uniform, and in some parts of the Southern Ocean, e.g., R02 in JAS, the averaged mixed-layer depth and the averaged vertical profile of NIE are very different. This is partly due to the fact that during separate high-NIE events, NIE within the mixed layer is not exactly vertically uniform (see Figure 10 which is discussed in detail in section 5.1). On the other hand, the apparent vertical shear of horizontally and temporally averaged NIE within the horizontally and temporally averaged depth of the mixed layer is probably not meaningful since it is an average over many different events.

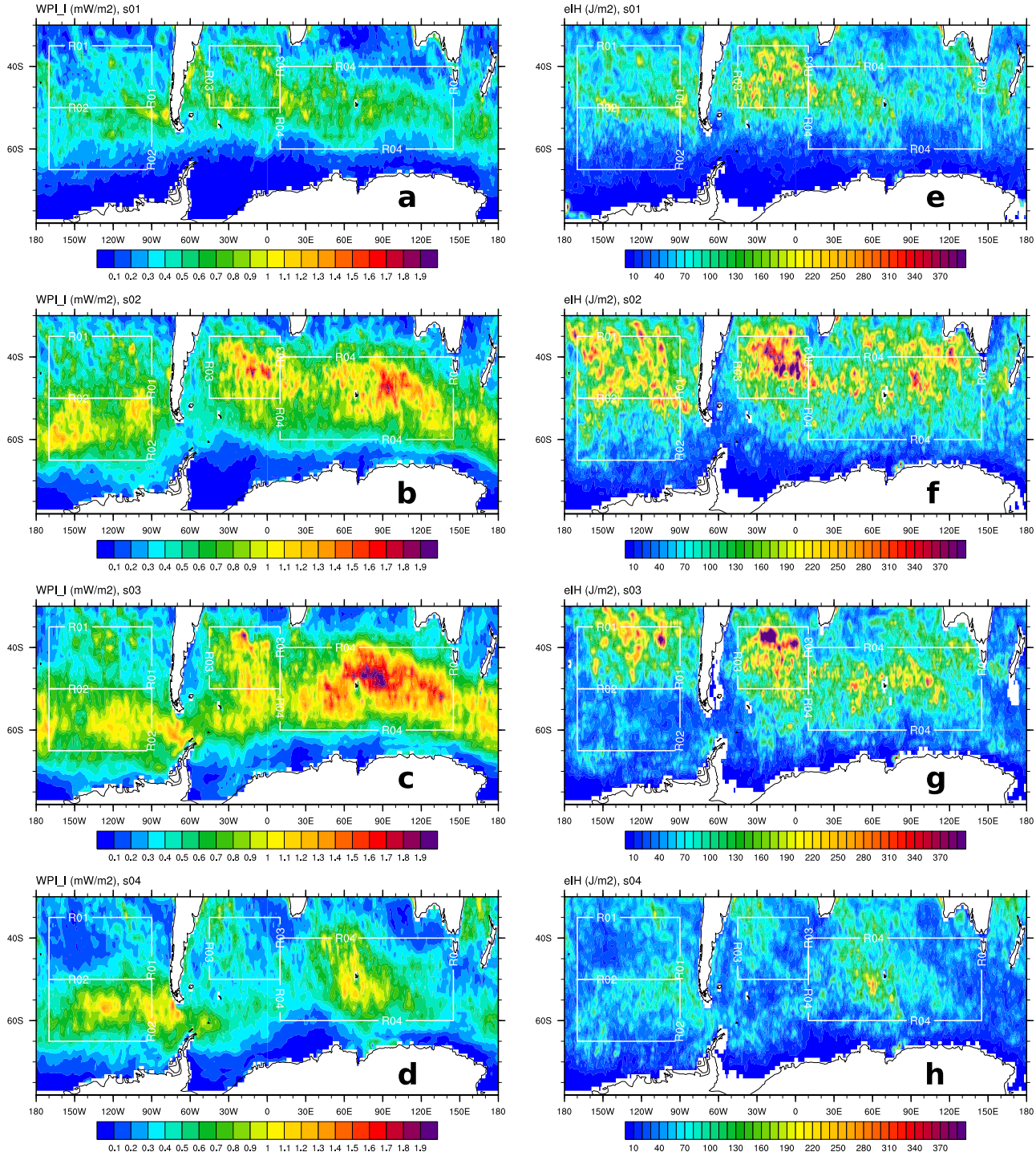

Figure 5. Seasonal averages of near-inertial WPI (mW/m^2) and mixed-layer NIE (J/m^2). (a–d) Near-inertial WPI (mW/m^2) for JFM, AMJ, JAS, and OND from 2001. (e–h) Mixed-layer NIE (J/m^2) for JFM, AMJ, JAS, and OND from 2001.

3.4. Trapping in Anticyclonic Eddies

[32] The vertical profiles of NIE shown in Figure 6 indicate that high levels of NIE are mainly found in the surface-mixed layer. However, among many others, *Kunze* [1985], *Zhai et al*. [2005], and *Zhai et al*. [2007] showed that in anticyclonic eddies, there can be enhanced downward propagation of NIE. They argue that it is the effective Coriolis parameter $f + \zeta/2$, where ζ is the relative vorticity, rather than the Coriolis parameter f alone that sets the frequency at which NIWs are excited. NIWs generated inside an anticyclonic (positive ζ in the southern hemisphere) eddy are then trapped inside of the eddy because they cannot propagate into the surrounding regions where the modulus of the effective Coriolis parameter is larger. Recent

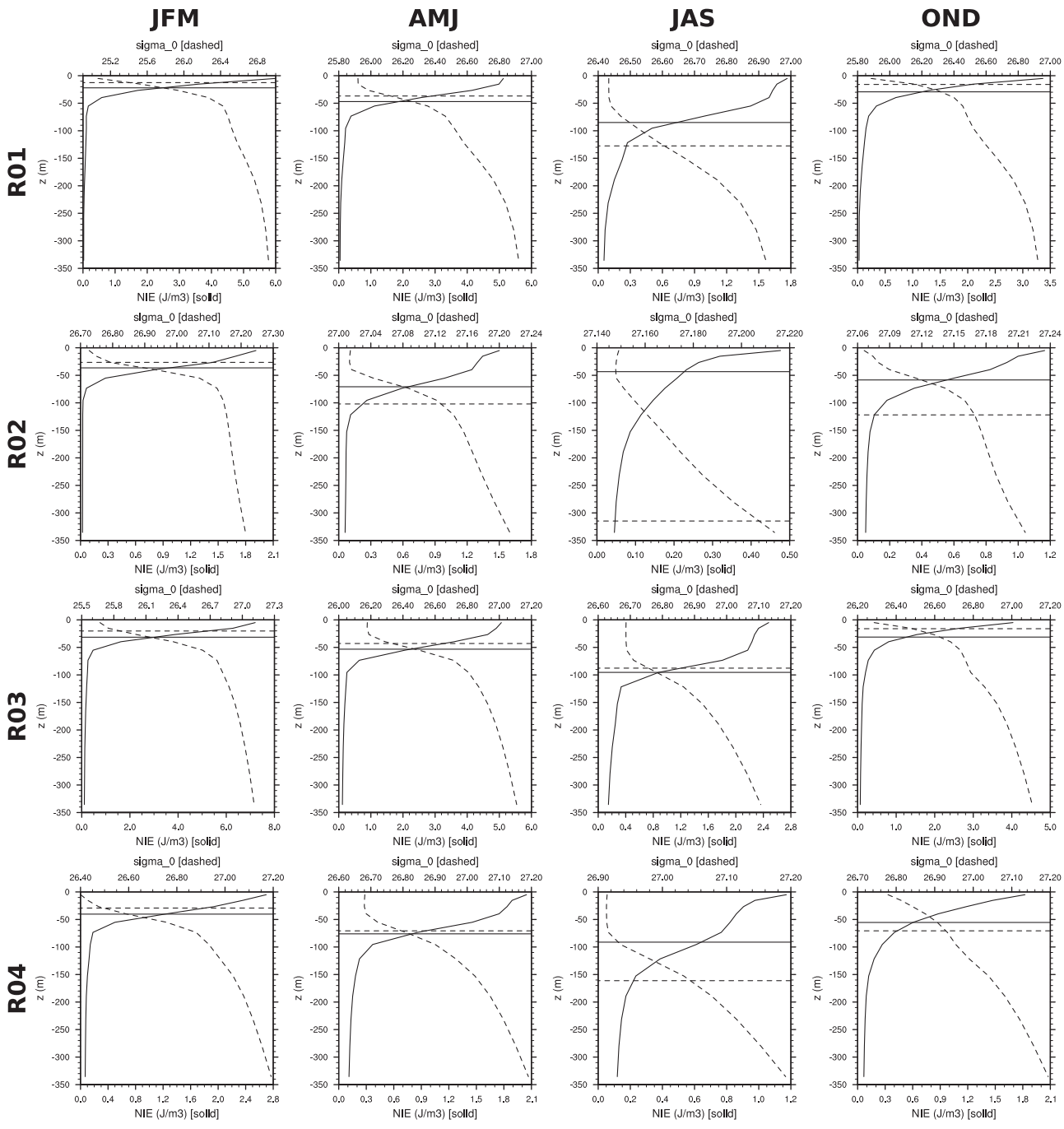

Figure 6. Horizontal averages of NIE (solid lines), and potential density referenced to the surface σ_0 (dashed lines) over the top 350 m of the water column together with horizontal averages of the penetration depth of NIE, $H_{E_{0.5}}$ (horizontal solid lines), and of the mixed-layer depth, H (horizontal dashed lines). The horizontal averages have been calculated for (top to bottom) the regions R01–R04 and for (left to right) the seasons JFM–OND. Note that the scales differ for each panel.

observations show further observational evidence for the trapping of NIE in anticyclonic eddies [*Jing et al.*, 2011; *Joyce et al.*, 2013].

[33] We use the high-resolution model output from the primitive-equation model that is available for the first 36.5 days of 2001 to show that there are strong local maxima of NIE at depth associated with strong anticyclonic eddies. Local maxima of NIE at depth are scattered all over the model domain. As an example, we examine the vertical distribution of NIE along a section in the South Atlantic. Figure 7a shows near-inertial energy E_I, subinertial relative vorticity $\zeta_S = (v_S)_x - (u_S)_y$, and $E_{rel} \equiv E_I/E_{I,smoothed}$ for a section at 49.9°S ranging from 30°W to 15°W. $E_{I,smoothed}$ denotes NIE that has been horizontally filtered with a $\pm 1°$

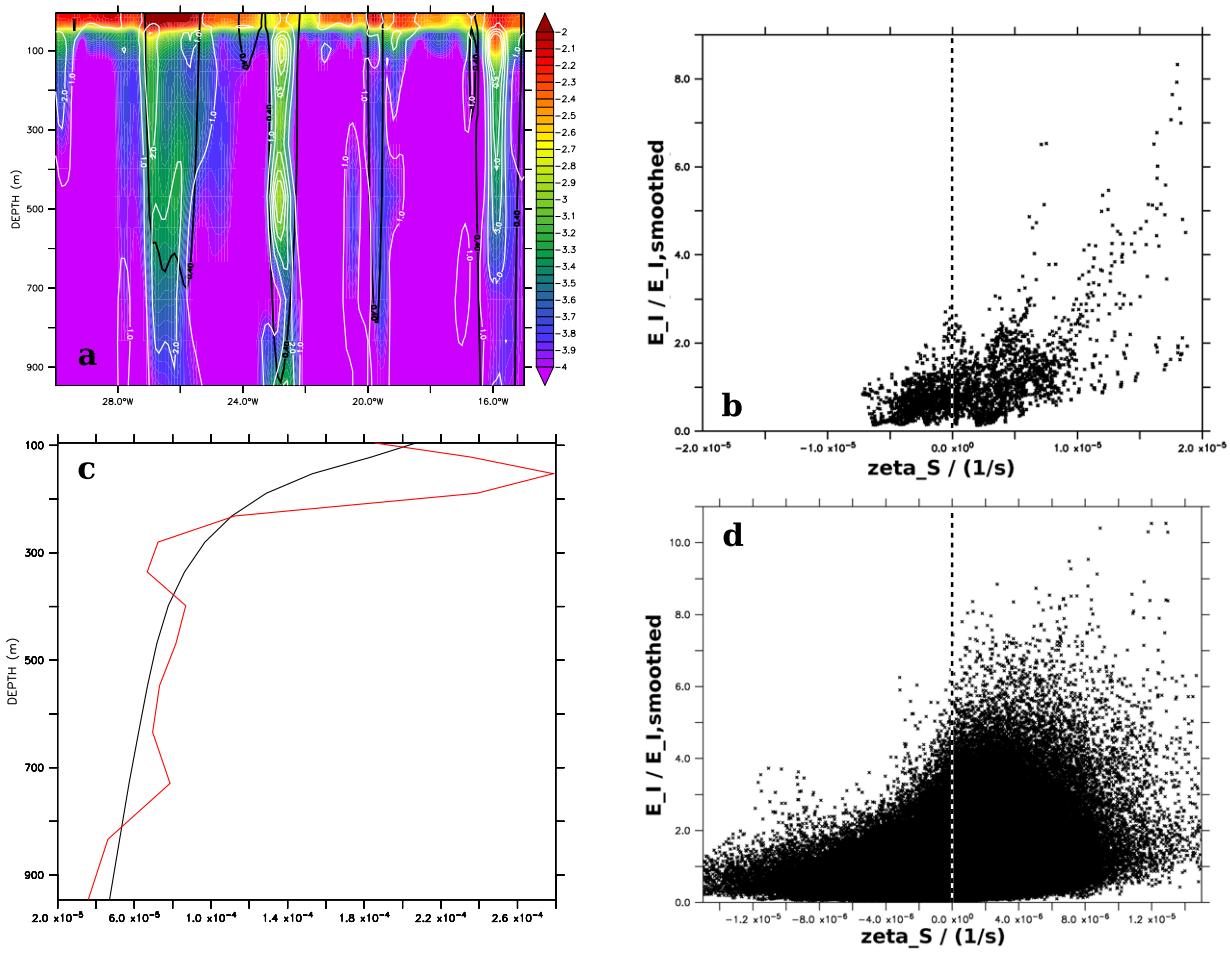

Figure 7. (a) Zonal section at 49.9°S. Colors show $\log_{10}(E_I)$, black contours show the 0.4×10^{-5}/s isoline of $\zeta_S \equiv (v_S)_x - (u_S)_y$, and white contours show E_{rel} which is a measure for the strength of local maxima (see text). High E_{rel} coincides with positive ζ_S at depth. (b) Scatterplot of E_{rel} versus ζ_S for the data shown in Figure 7a. The dashed line indicates zero relative vorticity. (c) Horizontal (whole model domain) average of NIE (m^2/s^2) using all grid points (black line) and using only grid points (red line) where ζ_S at the surface exceeds the value of 0.5×10^{-5}/s. (d) Same as Figure 7b except for the whole model domain and restricted to 1000 m depth. All data show time averages for the first 36.5 days of the year 2001.

$\times \pm 2^\circ$ (latitude $\times$ longitude) Hanning window. We use E_{rel} as a measure for the ratio of local NIE to the ambient NIE and hence as a measure for the strength of local maxima of NIE. From Figure 7a, it is evident that regions of high NIE coincide with regions of positive ζ_S at depth. To further confirm this, Figure 7b shows a scatterplot of E_{rel} and ζ_S for the section shown in Figure 7a covering all depths up to 1000 m, and Figure 7d shows the same scatterplot for the whole model domain and restricted to 1000 m depth. Local maxima of NIE ($E_{rel} > 1$) are almost exclusively associated with positive relative vorticity. Figure 7c compares the horizontally and temporally averaged NIE for the whole model domain to the horizontally and temporally averaged NIE for grid points where time-averaged surface relative vorticity ζ_S exceeds 0.5×10^{-5}/s. There is a clear enhancement of NIE inside anticyclonic eddies for depths around 200 m and again, around 700 m depth. The surface area with $\zeta_S \geq 0.5 \times 10^{-5}$/s is about 9.8% of the whole (water covered) model domain, while the same regions contribute 21.3% to the whole-model-domain horizontal integral of NIE at depths between 300 and 1000 m. We conclude that there is an enhancement NIE at depth in anticyclonic eddies and that this may play a significant role in providing energy that is available for mixing in the deep ocean. However, it should be remembered that the bulk of the wind-induced NIE in the ocean is, nevertheless, used to increase potential energy (by deepening the mixed-layer depth) or to produce heat (by dissipation within the mixed layer) and hence is unavailable for mixing at depth [*Furuichi et al.*, 2008; *Zhai et al.*, 2009].

4. Temporal Distribution of Near-Inertial Wind-Power Input and Near-Inertial Energy

[34] Figure 8 shows, for the year 2001, monthly-mean time series of near-inertial WPI, the amplitude of the near-

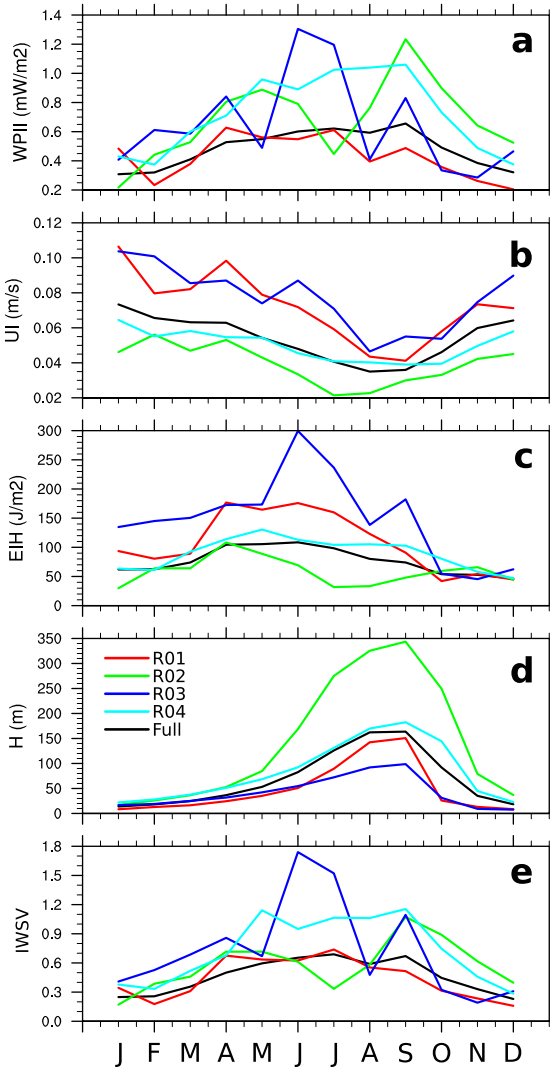

Figure 8. Monthly means of horizontal averages of (a) near-inertial WPI (mW/m^2), (b) amplitude of the near-inertial velocity at the surface (m/s), (c) mixed-layer NIE (J/m^2), (d) the mixed-layer depth (m), and (e) the inertial wind-stress variance (IWSV), for the regions R01 (red lines), R02 (green lines), R03 (blue lines), R04 (cyan lines), and for the full model domain (black lines).

inertial velocity at the surface, mixed-layer NIE, the mixed-layer depth, and the amplitude of the IWSV (see section 2.6) averaged over the whole model domain and averaged over the regions R01–R04 (see section 2.4). Near-inertial WPI shows a broad maximum during austral fall (AMJ) and winter (JAS) which is largely reflected by the mixed-layer NIE. Despite the stronger wind forcing in austral winter (JAS), the near-inertial velocity amplitudes at the surface are maximal in austral summer (JFM) and minimal in austral winter (JAS) when near-inertial WPI is spread over a deeper mixed layer. This agrees with the findings of *Chaigneau et al*. [2008] who present direct observational estimates for the annual cycles of near-inertial velocity amplitudes at the surface. In our model experiment, the mixed-layer NIE peaks in austral spring (AMJ). This is contrary to the indirect estimate of *Chaigneau et al*. [2008] who, due to the lack of direct global-scale estimates of NIE at depth, assume the near-inertial velocity amplitudes to be vertically uniform throughout the mixed layer. They therefore estimate mixed-layer NIE as the product of the surface NIE and the mixed-layer depth and hence find that mixed-layer NIE to peak in austral winter (JAS) when the mixed layer is deep. The remarkable similarity of the time series of IWSV and near-inertial WPI is discussed in detail in section 5.

5. The Relationship Between Near-Inertial Wind-Power Input, Near-Inertial Energy, and the Wind Forcing

[35] We seek to explain the relationship between the wind forcing at inertial time scales, IWSV, the modeled near-inertial WPI, and the amplitude of NIWs measured by the amplitude of the near-inertial velocity at the surface and the mixed-layer NIE.

5.1. Insensitivity of Near-Inertial Wind-Power Input to the Mixed-Layer Depth

[36] As pointed out above, horizontal averages of monthly-mean IWSV and of modeled monthly-mean near-inertial WPI shown in Figures 8a and 8e follow each other closely.

[37] Figure 9a shows a scatterplot of monthly-mean IWSV and near-inertial WPI averaged over bins of size 6° ×10° (latitude × longitude). Near-inertial WPI is almost proportional to IWSV with a slight damping for very high values of IWSV. This indicates that WPI is mainly determined by the strength of the near-inertial wind forcing. And in fact, near-inertial WPI divided by IWSV is largely independent of the prevailing mixed-layer depth (see Figure 9b).

[38] To understand this, we note that as for example, pointed out by *Plueddemann and Farrar* [2006], NIE is injected into the ocean mainly during strong events which often last for only a fraction of one inertial cycle, while the NIWs generated by such an event then decay on time scales typically of $O(5\text{days})$. To see this, Figure 10 shows the modeled response during a typical storm event leading to strong NIWs in the mixed layer. The oceanic response to the storm can be separated into two stages. During the first stage, which lasts only for a few hours, a strong wind forcing leads to near-inertial currents throughout the mixed layer (Figure 10b) which are, however, intensified toward the surface. The strong wind forcing leads to a deepening of the mixed layer (Figure 10a). As the wind forcing increases, the deepening of the mixed layer starts instantaneously. During the second stage, high levels of NIE are found throughout the mixed layer, and the vertical shear (Figure 10d) is small except at the base of the mixed layer. As long as here are enhanced levels of NIE, the mixed layer continues to deepen. The time average of the near-inertial WPI time series shown in Figure 10 is dominated by the strong positive contribution on 20 September, and this, in turn, is determined by the initial increase of $|\boldsymbol{u}_I|$ before NIE is spread to the mixed-layer base at a rate of approximately 5 m/h.

[39] Note that the event shown in Figure 10 is chosen as a representative example for many similar events scattered

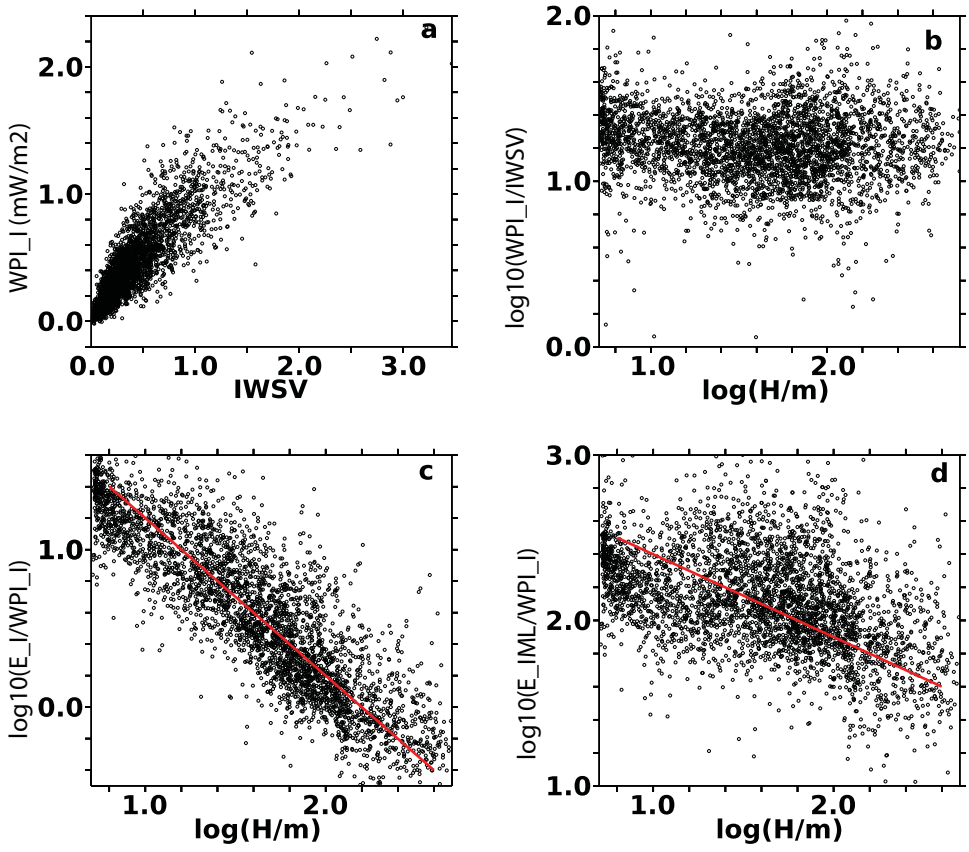

Figure 9. (a) IWSV (in arbitrary units) versus near-inertial WPI (in mW/m^2). (b) $\log_{10}$ of the mixed-layer depth, H, versus $\log_{10}$ of the ratio of IWSV and near-inertial WPI. (c) $\log_{10}$ of the mixed-layer depth, H, versus $\log_{10}$ of surface NIE divided by near-inertial WPI. The slope of the red line is -1. Hence, the data are compatible with $E_I(z{=}0) \propto WPI_I/H$. (d) $\log_{10}$ of the mixed-layer depth, H, versus $\log_{10}$ of mixed-layer NIE divided by near-inertial WPI. The slope of the red line is -0.5. Each point represents a monthly and a horizontal mean over a $6^\circ \times 10^\circ$ (latitude $\times$ longitude) bin.

all over the model domain and over the whole year 2001. The characteristics of all these events are similar: strong positive near-inertial WPI for a short time, often less than an inertial cycle, homogenization of $|\boldsymbol{u}_I|$ within the mixed layer, and subsequent decay of the then largely vertically uniform $|\boldsymbol{u}_I|$ in the surface-mixed layer. We note that this picture could depend on the vertical resolution of the model, but we do not believe the picture would change fundamentally if it were possible to repeat the model experiments at much increased vertical resolution.

[40] We conclude that the insensitivity of near-inertial WPI to the mixed-layer depth that we find in our model experiment can be explained by the fact that the vertical homogenization of $|\boldsymbol{u}_I|$ in the mixed layer happens on time scales similar to or larger than the duration of strong positive near-inertial WPI events.

5.2. Meridional Distribution of Inertial Wind-Stress Variability

[41] Figure 11a shows the sum of the zonally averaged spectral densities of the wind stress $\tilde{\tau}^x(\omega)$ and $\tilde{\tau}^y(\omega)$, together with the inertial frequency f. The contribution of wind stress to near-inertial WPI is set by the spectral density close to the inertial frequency, f, that is indicated by the thick black line. It is immediately clear that the fact that the NIWs at the ocean surface sample the wind stress at frequencies with weaker and weaker variability leads to a lower levels of WPI at high latitudes. This is not to be confused with the spurious underestimation of near-inertial variability in the ocean that arises from the finite sampling frequency of the six-hourly wind stress discussed in section 3.1.

[42] Figure 11b shows the zonal averages of IWSV, of temporally averaged near-inertial WPI, of the variance of the wind stress, and of the mean modulus of the wind stress all based on the six-hourly wind stress driving the primitive-equation model during the year 2001. The meridional maxima of IWSV and near-inertial WPI are shifted to the north compared to both the maximum of wind-stress variance and of the modulus of the wind stress. North of their maxima, IWSV and near-inertial WPI are generally larger than south of their maxima, while the wind-stress variance and the modulus of the wind stress are largely symmetric about 55°S. As was also noted by *Elipot and Lumpkin* [2008], there is a resonance between the inertial frequency and the diurnal cycle close to the northern boundary of the model domain at 30°S. This resonance is clearly visible in zonally averaged IWSV. In temporally and zonally averaged near-inertial WPI, the enhancement at 30°S is less pronounced.

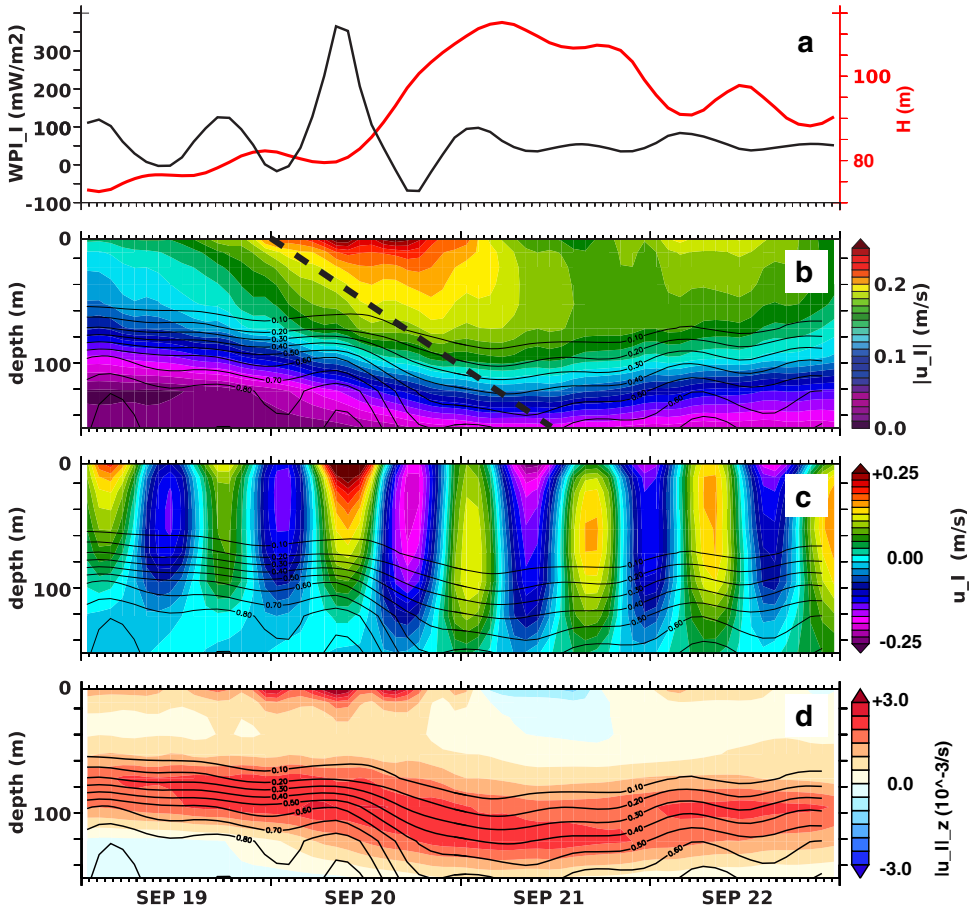

Figure 10. (a) The black line shows near-inertial WPI in 10^{-3} W/m^2. The red line shows the depth at which potential temperature deviates from its surface value by 0.3 K. (b) Colors show the near-inertial amplitude $|\boldsymbol{u}_I|$. Contours show the difference of potential temperature at depth to its surface value using a 0.1 K interval. The black dashed line has a slope of 100 m/24 h $\approx$ 5 m/h. (c) Colors show the zonal component of the near-inertial velocity u_I. The contours are the same as in Figure 10b. (d) Colors show the vertical shear of the inertial amplitude $|\boldsymbol{u}_I|$ in 10^{-3}/s. The contours are the same as in Figure 10b. All data are from 52°S and 136°E and cover the time from 19 to 22 September 2001.

5.3. The Influence of the Mixed-Layer Depth

[43] In the PM70 slab model (see section 2.3), the wind-power input term acts to accelerate currents that are uniformly distributed over the whole mixed-layer depth. Hence, NIE in the slab model is proportional to the inverse of the mixed-layer depth (see (9)). For the near-surface NIE shown in Figure 9c, the relation $E_I/WPI_I \propto H^{-1}$ from (9) is satisfied almost exactly. NIE integrated over the whole mixed-layer depth, $E_{I,ML}$, is still sensitive to a monotonically rising function of the inverse of the mixed-layer depth (Figure 9d compares the modeled $E_{I,ML}/WPI_I$ to $H^{-0.5}$), and the simple PM70 scaling (10), which predicts mixed-layer NIE to be independent of the mixed-layer depth, no longer holds. The meridional maximum of the mixed-layer depth (see Figure 1) approximately coincides with the meridional maximum of near-inertial WPI (see Figure 4a). Hence, the effect of near-inertial WPI on NIE close to its meridional maximum is reduced, and the meridional maximum of NIE at the surface and NIE integrated over the mixed layer (see Figure 4b) is found further north.

6. Recent Trends in the Wind Forcing and Their Implications for Near-Inertial Energy and Near-Inertial Wind-Power Input

[44] In this section, we examine recent decadal trends of the inertial variability of the wind forcing, as measured by IWSV defined in (11), to gain insight into decadal variability of near-inertial WPI and NIE in the Southern Ocean. As was shown in sections 4 and 5, near-inertial WPI almost exactly follows IWSV, at least for the seasonal cycle, and we assume that this relationship continues to hold on longer time scales.

[45] We diagnose IWSV as described in section 2.6 based on non-surface-velocity-dependent six-hourly ERA-Interim wind stress covering the years 1979–2011. In section 2.7, we showed that ERA-40 winds from the presatellite era (before 1979) produce much weaker high-frequency wind variability than those post-1979, and hence, should not be used to estimate high-frequency properties of the wind forcing.

[46] Figure 12 shows the annual cycle of IWSV based on the first 16 years and the last 16 years of ERA-Interim.

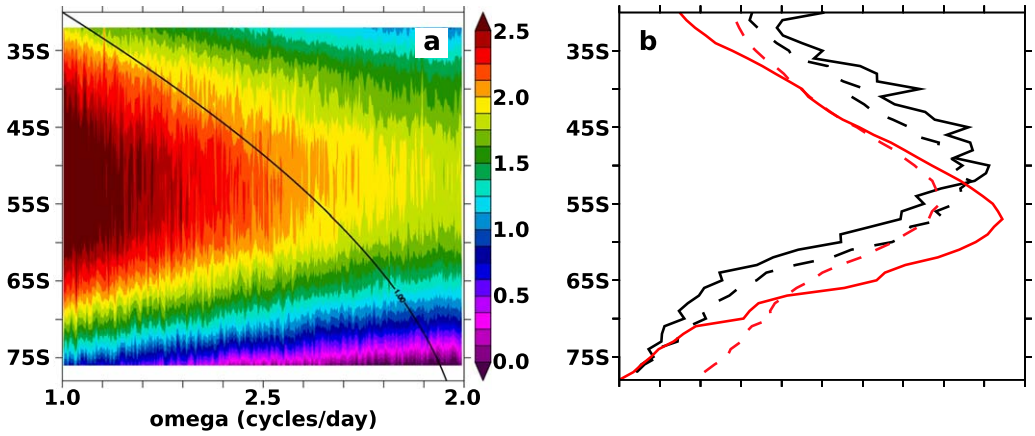

Figure 11. (a) Colors show zonally averaged spectral density of the wind stress $(\tilde{\tau}^x)^2+(\tilde{\tau}^y)^2$ in arbitrary units. The black line indicates the dependence of the modulus of the inertial frequency, f, depending on the latitude. (b) Zonal averages of the spectral density of the wind stress evaluated at the inertial frequency (solid black line), of time-averaged near-inertial WPI (dashed black line), of the variance of the wind stress (solid red line), and of the time average of the modulus of the wind stress (dashed red line). The zonal averages have been normalized by their meridional averages. All data are derived from the six-hourly wind stress of the year 2001 that is used to drive the primitive-equation model.

There is a general shift toward stronger IWSV in the second half of ERA-Interim. When averaged over the whole Southern Ocean south of 30°S, the increase of IWSV is bigger than two temporal standard deviations (based on monthly means) of the horizontally and monthly averaged data throughout the year.

[47] Figure 13 shows time series of IWSV split into the four seasons JFM, AMJ, JAS, and OND and into the four regions R01–R04 (see section 2.4) for the years 1979–2011 together with estimates of linear trends. We assess the significance of the trends using a bootstrap approach [*Efron and Tibshirani*, 1986] which we outline in the following. From the full time series, we draw 10^3 random subsamples $\{t^n, \mathrm{IWSV}\,(t^n)\}$, where t^n refers to real time, each of which has the same length as the full time series, but may have doublers. Then, for each subsample indicated by the superscript n, the linear trend S^n is estimated as

$$S^n = \frac{\overline{(t^n)'(\mathrm{IWSV}\,(t^n))'}}{\overline{(t^n)'^2}}, \tag{12}$$

where $\overline{(\ldots)}$ denotes a time average which is applied separately to each subsample, and the prime denotes a deviation thereof. We estimate the trend of the full time series as the mean of all S^n and error of S as the standard deviation of all S^n.

[48] Horizontally averaged IWSV based on ERA-Interim winds shows a significant upward trend for all four seasons if averaged over the whole Southern Ocean south of 30°S. Split into different regions, the picture is more diverse, but upward trends of IWSV prevail. Table 1 lists relative increases of IWSV associated with the trend estimates for the 33 years covered by ERA-Interim. Averaged over the full model domain, annual-mean IWSV increased by (16.4 ± 2.2)%. In R01 and R02, the increases of annual-mean IWSV were stronger (25.2% and 39.8%) than averaged over the whole domain, and in R04, the increases were lower (13.1%) than averaged over the whole domain. Annual-mean IWSV in R03 does not show a significant trend.

[49] Figure 14a shows the regression of annual-mean IWSV onto the annual-mean SAM index (see section 2.8). A positive SAM index is associated with enhanced IWSV south of approximately 50°S and reduced IWSV north of 50°S. The strongest SAM-related increase of IWSV is found over the Pacific sector of the ACC, which roughly corresponds to our region R02 and which also shows the strongest positive trend of annual-mean IWSV (Figure 14b). The modulus of the correlation of the detrended time series of the annual-mean SAM index and the annual-mean IWSV can be understood as a measure of the fraction of interannual variability of IWSV associated with the SAM. Over the Pacific sector of the ACC (R02), the strong positive trend of IWSV and a high correlation (between 0.5 and more than 0.8) of IWSV and the SAM index coincide. Over the other regions, the spatial distribution of the correlation between the SAM and IWSV is noisy. Comparison of basinwide and regional averages of annual-mean IWSV (Figure 15) further supports the picture that in R02, it is the gradual shift to a more positive SAM index during the last three decades [*Marshall*, 2003; *Swart and Fyfe*, 2012] that drives the stronger IWSV. In the other regions and in the whole model domain, only years of very strong positive or negative SAM index leave their signature in annual-mean IWSV (see, e.g., the years 1998 and 1999).

[50] Given the fact that the modeled near-inertial WPI very closely follows IWSV on monthly to seasonal time scales, and given the insensitivity of near-inertial WPI to the mixed-layer depth (see section 5.1), we conclude that near-inertial WPI over the Southern Ocean has undergone a significant upward trend during the last three decades. Figures 14 and 15 indicate that if the positive SAM trend continues as proposed by climate projections for the 21st

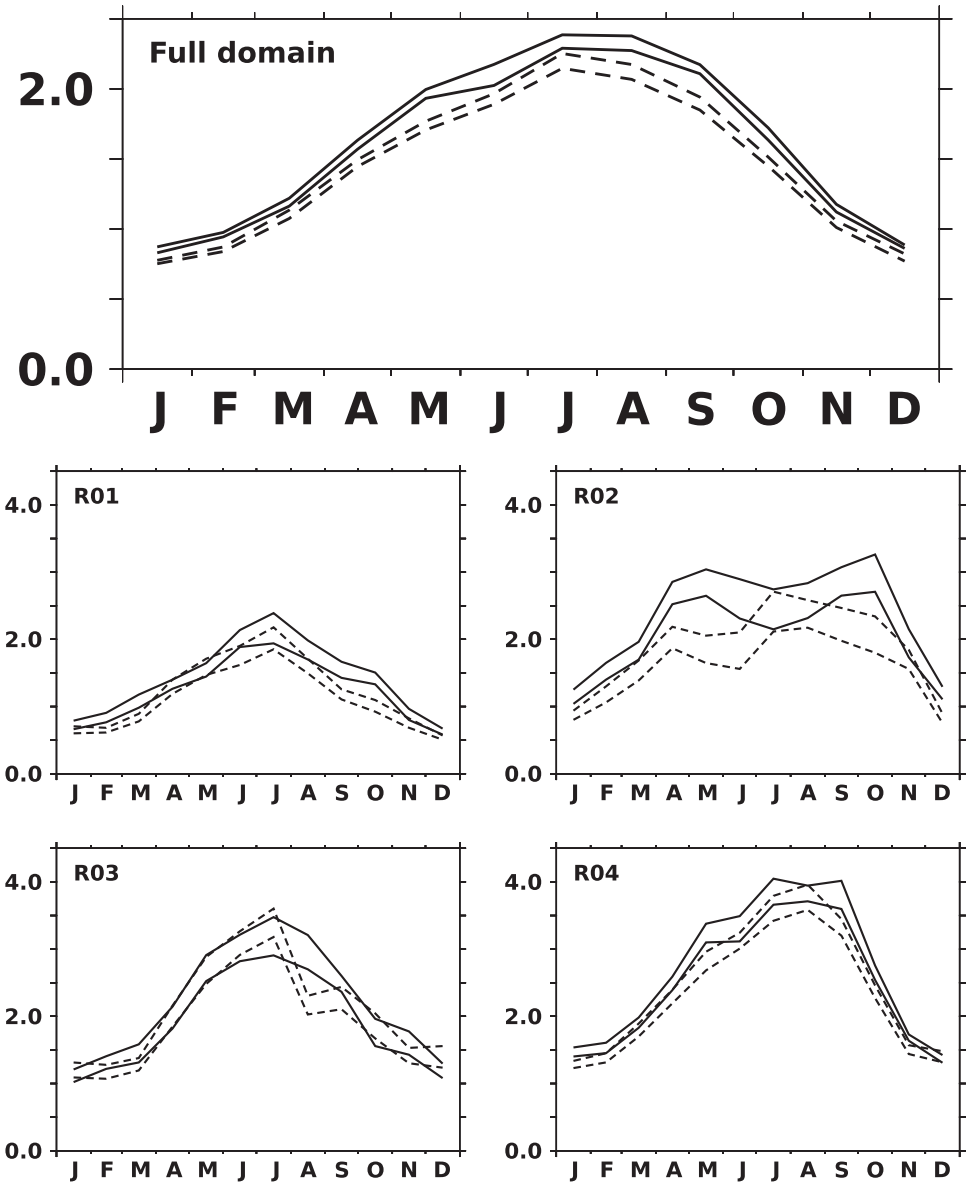

Figure 12. Annual cycles of the horizontal averages of IWSV for the last 16 years of ERA-Interim (solid lines) and for the first 16 years of ERA-Interim (dashed lines). The top and bottom lines show the annual cycle ± 1 standard deviation (see text). (left to right) IWSV is averaged over the full domain and over the regions R01–R04.

century [*Swart and Fyfe*, 2012], IWSV and hence near-inertial WPI especially in R02 are likely to increase as well.

[51] On the other hand, mixed-layer NIE and NIE at the surface are sensitive to the mixed-layer depth. *Sallee et al*. [2010] present observational evidence that the mixed-layer depth responds to changes in the SAM in a zonally asymmetric way. They find that the mixed-layer-depth anomaly associated to ±1 standard deviation of the SAM index can be as big as ±100 m in the eastern Indian Ocean and in the central Pacific Ocean which correspond to parts of our regions R04 and R02. The upward trend of the SAM index in recent decades [*Marshall*, 2003; *Swart and Fyfe*, 2012] that is also visible in Figure 15 is associated with a deepening of the mixed layer which may partly compensate the effect of increased IWSV and near-inertial WPI on mixed-layer and near-surface NIE in our region R02. In fact, one might hypothesize that at least part of the observed SAM-related mixed-layer deepening is due to the enhanced IWSV [*Pollard et al*., 1972].

7. Summary and Conclusions

[52] In section 3, we highlighted the spatial distribution of time-averaged near-inertial WPI and NIE. While near-inertial WPI shows a large-scale zonal structure with meridional maxima between 65°S and 40°S that is superimposed by many smaller hot spots, mixed-layer NIE does not reflect the largely zonal structure of near-inertial WPI but agrees in the distribution of the smaller hot spots. In the

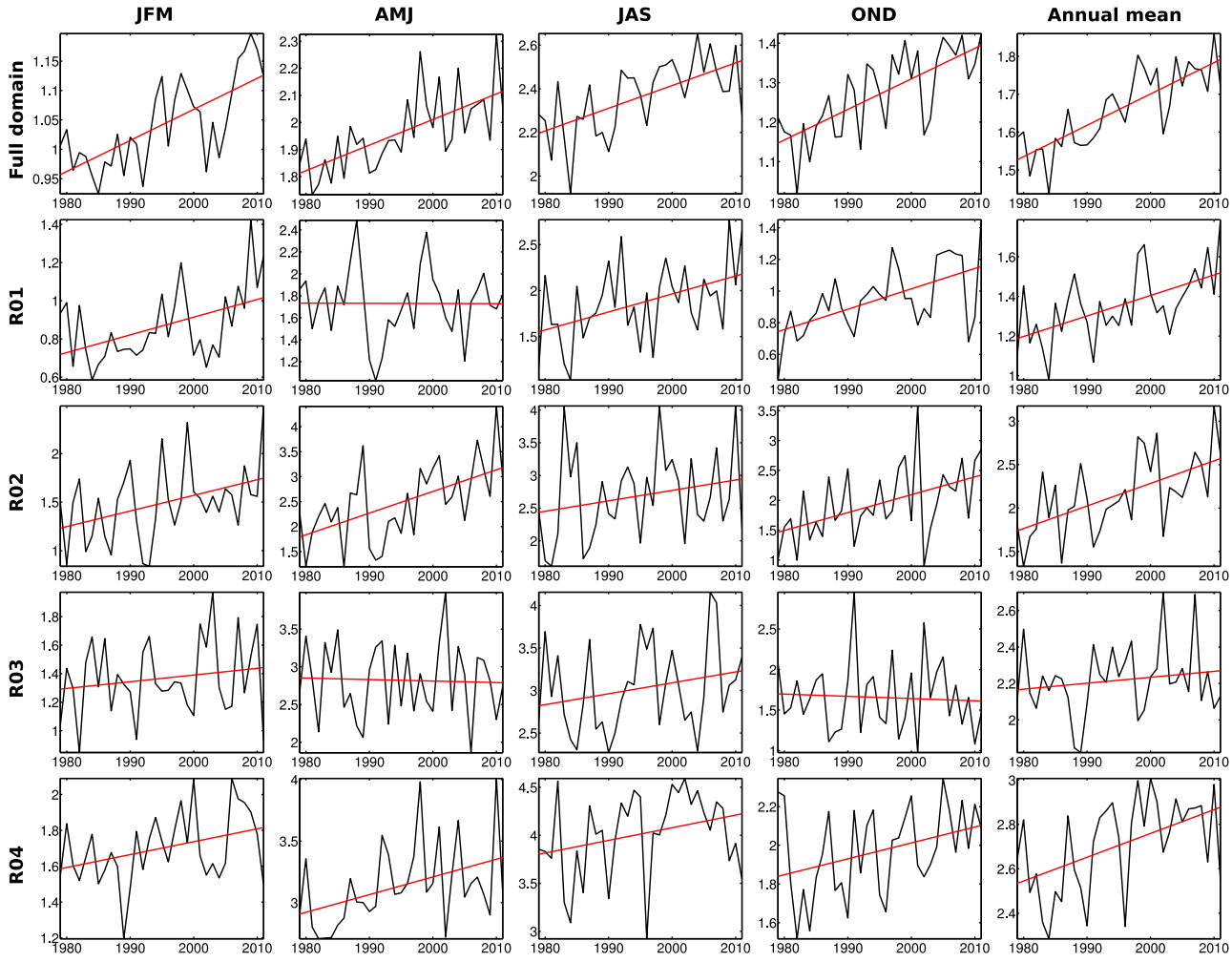

Figure 13. Seasonal and horizontal averages of IWSV together with the linear trends measured as the mean of an $N = 10^3$ bootstrap ensemble (see text). (top to bottom) Full domain and R01–R04. (left to right) JFM, AMJ, JAS, OND, and annual average.

vertical, we found that there generally is a separation into a surface layer with high levels of NIE and the interior ocean with much lower NIE, while the near-inertial velocity within the mixed layer is not exactly uniform. Furthermore, we showed that there is a clear enhancement of NIE at depth, which is almost exclusively associated to the presence of anticyclonic relative vorticity.

[53] In section 4, we examined horizontal averages of monthly-mean near-inertial WPI and NIE. While near-inertial WPI and mixed-layer NIE show broad maxima during austral fall and winter, which largely follow the increased inertial wind-stress variability (IWSV), the near-surface near-inertial amplitudes are maximal in austral summer and spring when NIE injected at the surface spreads over a shallower mixed layer.

[54] We sought to systematize the relation between wind forcing at the inertial frequency and near-inertial WPI and NIE in section 5. The modeled near-inertial WPI was found to very closely follow IWSV and to be largely insensitive of the mixed-layer depth. Thus, we attributed to the fact that near-inertial WPI is injected into the ocean mainly by strong events which often last only for a few hours, while the vertical homogenization of NIE within the mixed layer is determined by longer time scales. Hence, time-averaged near-inertial WPI is determined by the strong events and is insensitive to the mixed-layer depth. On the other hand, time-averaged NIE at the surface was shown to be sensitive to the mixed-layer depth with larger values of near-surface NIE for shallower mixed layers. This is because after the short resonant events of strong near-inertial WPI, NIE decays on time scales of several days and feels the influence of the mixed-layer depth. We found that both IWSV

Table 1. Slopes $S \pm \sigma_S$ of the Linear Fits Shown in Figure 13[a]

	JFM	AMJ	JAS	OND	Annual Mean
Full	16.8 ± 2.8	15.7 ± 3.1	14.7 ± 3.8	20.1 ± 3.1	16.4 ± 2.2
R01	35.2 ± 13.3	-0.6 ± 8.0	35.1 ± 12.0	44.3 ± 13.5	25.2 ± 6.8
R02	34.7 ± 14.0	58.5 ± 13.8	19.5 ± 16.1	50.4 ± 14.4	39.8 ± 9.3
R03	11.6 ± 13.0	-0.9 ± 9.7	14.0 ± 9.7	-5.1 ± 12.4	4.8 ± 4.8
R04	14.3 ± 6.5	15.0 ± 6.0	10.8 ± 6.1	13.6 ± 6.8	13.1 ± 4.0

[a]Shown is the ratio of the increase or decrease of IWSV associated with the slope acting for 33 years relative to the temporal mean over 33 years in percent.

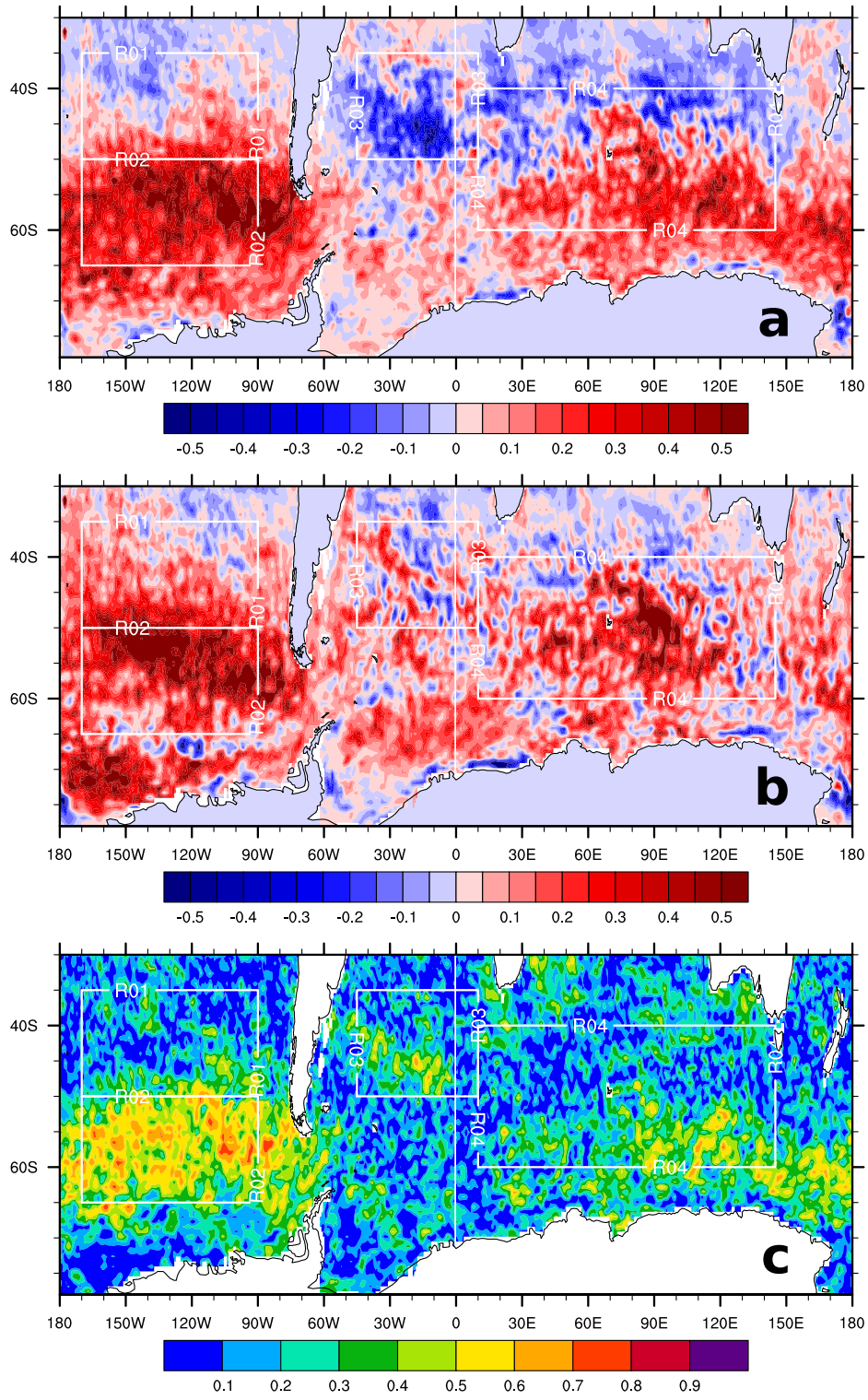

Figure 14. (a) SAM-related IWSV pattern. (b) Trend of IWSV over the whole ERA-Interim record. (c) Modulus of the correlation of IWSV to the SAM index. Assuming that all years are independent, the critical correlation for 95% confidence is 0.34. All data are based on the annual-mean SAM index and annual-mean IWSV.

and the closely related near-inertial WPI are maximal north of the latitudes of the strongest mean wind stress and of the strongest wind-stress variability integrated over the whole frequency domain. We explained this asymmetry by the fact that the inertial frequency depends on the latitude and that hence, the wind stress is sampled at frequencies with less and less variability the higher the latitude.

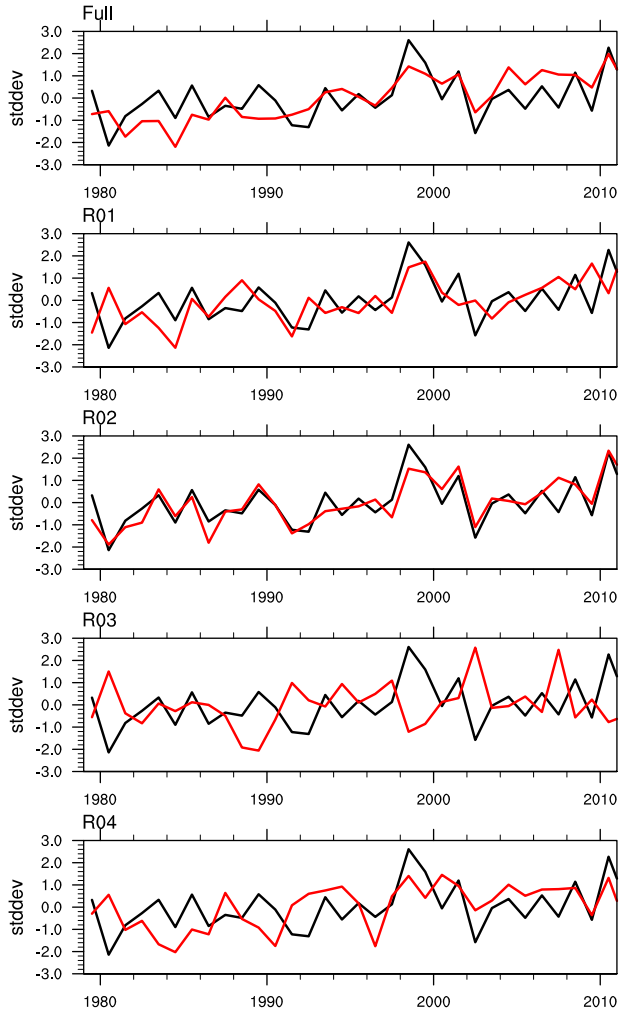

Figure 15. Annual-mean SAM index (black lines) and horizontally averaged annual-mean IWSV (red lines) for the full model domain and for the regions R01–R04. The time series of horizontally averaged annual-mean IWSV has been normalized to yield zero mean and unit standard deviation.

[55] In section 6, we examined trends of IWSV based on the ERA-Interim reanalysis, which covers the last three decades (1979–2011), and found annual-mean IWSV averaged over the whole model domain to increase by $(16.4 \pm 2.2)\%$. In the South Pacific and in the Pacific sector of the ACC, annual-mean IWSV increased by 25.2% and 39.8%, respectively. Furthermore, we showed that on interannual to decadal time scales, IWSV in the Pacific sector of the ACC (region R02) is largely determined by the SAM index. Assuming that the close relationship between IWSV and modeled near-inertial WPI, which was found for monthly to seasonal time scales, also holds on decadal time scales, we concluded that in the last three decades, near-inertial WPI also significantly increased. The implications for NIE, however, depend on decadal variability of the mixed-layer depth. *Sallee et al*. [2010] present evidence for a recent zonally asymmetric change of the mixed-layer depth that is associated to the increase of the SAM index over the last three decades. They show that a positive SAM leads to a deepening of the mixed layer in the Pacific sector of the ACC (our region R02), where we found the largest SAM-related and the largest overall increase of IWSV. Hence, in R02, the effect of increased mixed-layer depth and increased IWSV on NIE may at least partly compensate.

[56] Our results highlight the importance of knowledge about the time dependence of the vertical distribution of NIE and about the vertical spreading of NIE, which directly affect the magnitude of near-inertial WPI, and hence are critical to the levels of NIE in the ocean. While there are global-scale observational estimates of near-inertial amplitudes at the surface [*Chaigneau et al*., 2008; *Elipot and Lumpkin*, 2008], direct observations of near-inertial WPI and of the vertical distribution of NIE which could shed light on the relation of near-inertial WPI and IWSV are restricted to measurements in a few locations.

[57] **Acknowledgments.** W.R. and R.J.G. thank the DFG for support under the grant *Influence of the ocean surface velocity dependence of the wind stress on the dynamics of the Southern Ocean*. Thanks also to GEOMAR for continuing support and to the University Computing Center of the University of Kiel. W.R. thanks Lars Czeschel and Carsten Eden for providing initial help with the primitive-equation model. The authors thank three anonymous reviewers for their insightful comments that lead to a much improved manuscript.

References

Alford, M. (2003), Improved global maps and 54-year history of wind-work on ocean inertial motions, *Geophys. Res. Lett.*, *30*(8), 1424, doi:10.1029/2002GL016614.

Barnier, B., L. Siefridt, and P. Marchesiello (1995), Thermal Forcing for a global ocean circulation model using a 3-year climatology of ECMWF analyses, *J. Mar. Syst.*, *6*(4), 363–380, doi:10.1016/0924-7963(94)00034-9.

Blanke, B., and P. Delecluse (1993), Variability of the tropical Atlantic Ocean simulated by a general-circulation model with 2 different mixed-layer physics, *J. Phys. Oceanogr.*, *23*(7), 1363–1388, doi:10.1175/1520-0485(1993)023<1363:VOTTAO>2.0.CO;2.

Chaigneau, A., O. Pizarro, and W. Rojas (2008), Global climatology of near-inertial current characteristics from Lagrangian observations, *Geophys. Res. Lett.*, *35*, L13603, doi:10.1029/2008GL034060.

D'Asaro, E. (1985), The energy flux from the wind to near-inertial motions in the surface mixed layer, *J. Phys. Oceanogr.*, *15*(8), 1043–1059, doi:10.1175/1520-0485(1985)015<1043:TEFFTW>2.0.CO;2.

de Boyer Montegut, C., G. Madec, A. Fischer, A. Lazar, and D. Iudicone (2004), Mixed layer depth over the global ocean: An examination of profile data and a profile-based climatology, *J. Geophys. Res.*, *109*, C12003, doi:10.1029/2004JC002378.

Donelan, M., B. Haus, N. Reul, W. Plant, M. Stiassnie, H. Graber, O. Brown, and E. Saltzman (2004), On the limiting aerodynamic roughness of the ocean in very strong winds, *Geophys. Res. Lett.*, *31*, L18306, doi:10.1029/2004GL019460.

Duhaut, T., and D. Straub (2006), Wind stress dependence on ocean surface velocity: Implications for mechanical energy input to ocean circulation, *J. Phys. Oceanogr.*, *36*(2), 202–211, doi:10.1175/JPO2842.1.

Eden, C. (2006), Thickness diffusivity in the Southern Ocean, *Geophys. Res. Lett.*, *33*, L11606, doi:10.1029/2006GL026157.

Efron, B., and R. Tibshirani (1986), Bootstrap methods for standard errors, confidence intervals, and other measures of statistical accuracy, *Stat. Sci.*, *1*(1), 54–77.

Elipot, S., and R. Lumpkin (2008), Spectral description of oceanic near-surface variability, *Geophys. Res. Lett.*, *35*, L05606, doi:10.1029/2007GL032874.

Furuichi, N., T. Hibiya, and Y. Niwa (2008), Model-predicted distribution of wind-induced internal wave energy in the world's oceans, *J. Geophys. Res.*, *113*, C09034, doi:10.1029/2008JC004768.

Gaspar, P., Y. Gregoris, and J. Lefevre (1990), A simple eddy kinetic-energy model for simulations of the oceanic vertical mixing—Tests at

station Papa and Long-Term Upper Ocean Study Site, *J. Geophys. Res.*, *95*(C9), 16,179–16,193, doi:10.1029/JC095iC09p16179.

Gong, D., and S. Wang (1999), Definition of Antarctic Oscillation Index, *Geophys. Res. Lett.*, *26*(4), 459–462, doi:10.1029/1999GL900003.

Jiang, J., Y. Lu, and W. Perrie (2005), Estimating the energy flux from the wind to ocean inertial motions: The sensitivity to surface wind fields, *Geophys. Res. Lett.*, *32*, L15610, doi:10.1029/2005GL023289.

Jing, Z., L. Wu, L. Li, C. Liu, X. Liang, Z. Chen, D. Hu, and Q. Liu (2011), Turbulent diapycnal mixing in the subtropical northwestern Pacific: Spatial-seasonal variations and role of eddies, *J. Geophys. Res.*, *116*, C10028, doi:10.1029/2011JC007142.

Jochum, M., B. P. Briegleb, G. Danabasoglu, W. G. Large, N. J. Norton, S. R. Jayne, M. H. Alford, and F. O. Bryan (2013), The impact of oceanic near-inertial waves on climate, *J. Clim.*, *26*(9), 2833–2844, doi:10.1175/JCLI-D-12-00181.1.

Joyce, T. M., J. M. Toole, P. Klein, and L. N. Thomas (2013), A near-inertial mode observed within a Gulf Stream warm-core ring, *J. Geophys. Res.*, *118*(4), 1797–1806, doi:10.1002/jgrc.20141.

Kunze, E. (1985), Near-inertial wave-propagation in geostrophic shear, *J. Phys. Oceanogr.*, *15*(5), 544–565, doi:10.1175/1520-0485(1985)015<0544:NIWPIG>2.0.CO;2.

Large, W., and S. Pond (1981), Open ocean momentum flux measurements in moderate to strong winds, *J. Phys. Oceanogr.*, *11*(3), 324–336, doi:10.1175/1520-0485(1981)011<0324:OOMFMI>2.0.CO;2.

Marshall, G. (2003), Trends in the southern annular mode from observations and reanalyses, *J. Clim.*, *16*(24), 4134–4143.

Munk, W., and C. Wunsch (1998), Abyssal recipes: II. Energetics of tidal and wind mixing, *Deep Sea Res.*, Part I, *45*(12), 1977–2010, doi:10.1016/S0967-0637(98)00070-3.

Niwa, Y., and T. Hibiya (1999), Response of the deep ocean internal wave field to traveling midlatitude storms as observed in long-term current measurements, *J. Geophys. Res.*, *104*(C5), 10,981–10,989, doi:10.1029/1999JC900046.

Pacanowski, R. C. (1996), MOM 2 documentation, User's guide and reference manual, *Tech. Rep. 3*, Ocean Group, Geophys. Fluid Dyn. Lab., Princeton, N. J.

Plueddemann, A., and J. Farrar (2006), Observations and models of the energy flux from the wind to mixed-layer inertial currents, *Deep Sea Res., Part II*, *53*(1–2), 5–30, doi:10.1016/j.dsr2.2005.10.017, *in International Conference on Ocean Mixing*, Victoria, Canada, Oct. 11–14, 2004.

Pollard, R., and R. Millard (1970), Comparison between observed and simulated wind-generated inertial oscillations, *Deep Sea Res. Oceanogr. Abstr.*, *17*(4), 813–816, IN5, 817–821, doi:10.1016/0011-7471(70)90043-4.

Pollard, R. T., P. B. Rhines, and R. O. R. Y. Thompson (1972), The deepening of the wind-mixed layer, *Geophys. Fluid Dyn.*, *4*(1), 381–404, doi:10.1080/03091927208236105.

Price, J., R. Weller, and R. Pinkel (1986), Diurnal cycling—Observations and models of the upper ocean response to diurnal heating, cooling, and wind mixing, *J. Geophys. Res.*, *91*(C7), 8411–8427, doi:10.1029/JC091iC07p08411.

Rath, W., R. J. Greatbatch, and X. Zhai (2013), Reduction of near-inertial energy through the dependence of wind stress on the ocean-surface velocity, *J. Geophys. Res.*, *118*(6), 2761–2773, doi:10.1002/jgrc.20198.

Sallee, J. B., K. G. Speer, and S. R. Rintoul (2010), Zonally asymmetric response of the Southern Ocean mixed-layer depth to the Southern Annular Mode, *Nat. Geosci.*, *3*(4), 273–279, doi:10.1038/NGEO812.

Swart, N. C., and J. C. Fyfe (2012), Observed and simulated changes in the southern hemisphere surface westerly wind-stress, *Geophys. Res. Lett.*, *39*, L16711, doi:10.1029/2012GL052810.

Uppala, S., et al. (2005), The ERA-40 re-analysis, *Q. J. R. Meteorol. Soc.*, *131*(612, Part B), 2961–3012, doi:10.1256/qj.04.176.

Visbeck, M. (2009), A station-based Southern Annular Mode Index from 1884 to 2005, *J. Clim.*, *22*(4), 940–950, doi:10.1175/2008JCLI2260.1.

Watanabe, M., and T. Hibiya (2002), Global estimates of the wind-induced energy flux to inertial motions in the surface mixed layer, *Geophys. Res. Lett.*, *29*(8), 1239, doi:10.1029/2001GL014422.

Zhai, X., R. Greatbatch, and J. Zhao (2005), Enhanced vertical propagation of storm-induced near-inertial energy in an eddying ocean channel model, *Geophys. Res. Lett.*, *32*, L18602, doi:10.1029/2005GL023643.

Zhai, X., R. J. Greatbatch, and C. Eden (2007), Spreading of near-inertial energy in a 1/12 degrees model of the North Atlantic Ocean, *Geophys. Res. Lett.*, *34*, L10609, doi:10.1029/2007GL029895.

Zhai, X., R. J. Greatbatch, C. Eden, and T. Hibiya (2009), On the loss of wind-induced near-inertial energy to turbulent mixing in the upper ocean, *J. Phys. Oceanogr.*, *39*, 3040–3045, doi:10.1175/2009JPO4259.1.